

<https://doi.org/10.1038/s43247-024-01357-z>

Atmospheric river activity during the late Holocene exceeds modern range of variability in California

Check for updates

Clarke A. Knight , Lysanna Anderson , Liubov Presnetsova , Marie Champagne & David Wahl

Atmospheric rivers are associated with some of the largest flood-producing precipitation events in western North America, particularly California. Insight into past extreme precipitation can be reconstructed from sedimentary archives on millennial timescales. Here we document atmospheric river activity near Leonard Lake, California, over 3,200 years, using a key metric of atmospheric river intensity, that is silicon/aluminum enriched layers that are highly correlated with modern records of integrated vapor transport. The late twentieth century had the highest median integrated vapor transport since the onset of the Medieval Climate Anomaly, with integrated vapor transport increasing during the Little Ice Age. The reconstruction suggests California has experienced pluvial episodes that exceeded any in the meteorologic instrumental era, with the largest episodes occurring two and three millennia ago. These results provide critical data to help avoid underestimation of potential risks and aid future planning scenarios.

Atmospheric rivers (ARs)—filaments of concentrated moisture that deliver water to the midlatitudes' western coasts in both the northern and southern hemispheres^{1,2}—can produce heavy rainfall³, generating floods, landslides, and other catastrophic damage affecting people and property⁴. In recent decades, ARs have been associated with some of the largest flood-producing precipitation events in western North America³, particularly in California, where hydrologic impacts of ARs are enhanced by the abrupt topography of the Sierra Nevada range⁵. As the largest primary storm mechanism in California, the difference of a few large AR storms in a year dramatically changes precipitation totals and drives the state towards surfeit or drought⁶. For example, during the winter of 2022–2023, California experienced 31 AR storms⁷, resulting in an extraordinary snowpack, replenishing reservoirs⁸, and ending drought conditions across most of the state⁹. The AR storms also prompted a Major Disaster declaration due to the subsequent flooding, landslides, and mudslides across 47 counties¹⁰.

Climate models indicate an increasing likelihood of extreme precipitation events in California, including a 50% increase in runoff, via strengthening of AR activity^{11,12} with implications for flood and emergency management¹³. However, considerable uncertainty remains in flood hazard projections partly because of temporally limited instrumental data¹⁴. Lake sediments provide a natural archive that documents past local and regional precipitation events beyond instrumental and historical records, aiding our understanding of long-term climate–flood linkages¹⁵. With few exceptions¹⁶,

lacustrine data in California chronicle centennial to millennial-scale pluvial events from the Sierra Nevada¹⁷ and southern California^{18,19} but lack the temporal resolution to capture shorter-term events.

A major challenge for detecting paleo-AR activity is the lack of high temporal resolution sediment records that contain identifiable extreme precipitation deposits. A “fingerprint” of extreme events can be developed using a combination of lithological, grain size, and geochemical data with robust age control¹⁵, all of which are employed in this study. Previous research indicates extreme precipitation generates runoff with elevated concentrations of siliciclastic elements (i.e., high Si, Ti, Al) that can, in turn, correspond to clay deposition^{20–23}. Here we present a 3200-year record of extreme precipitation from a well-dated, high-temporal resolution sediment core from Leonard Lake, Mendocino County, California (123°21'48”W, 39°16'21”N; 613 m a.s.l.) (Fig. 1a). Leonard Lake is the largest natural freshwater lake in Mendocino County, California²⁴, with a watershed encompassing ~100 ha (Fig. 1b), and a surface area of ~6.5 ha with a maximum depth of around 16 m (Fig. 1c). Leonard Lake is an optimal site for reconstructing past extreme precipitation because it is 20 miles from the coast in a steep sided basin and located in the latitudinal zone of the highest frequency landfall for modern ARs along the west coast of North America²⁵. We reconstructed AR-related metrics using a calibration-in-time approach^{26,27} to develop a model between extreme precipitation (instrumental record), and Si/Al values and percent clay (proxy data) in the

U.S. Geological Survey, NASA Ames Research Park, Mountain View, CA 94035, USA.

 e-mail: cknight@usgs.gov

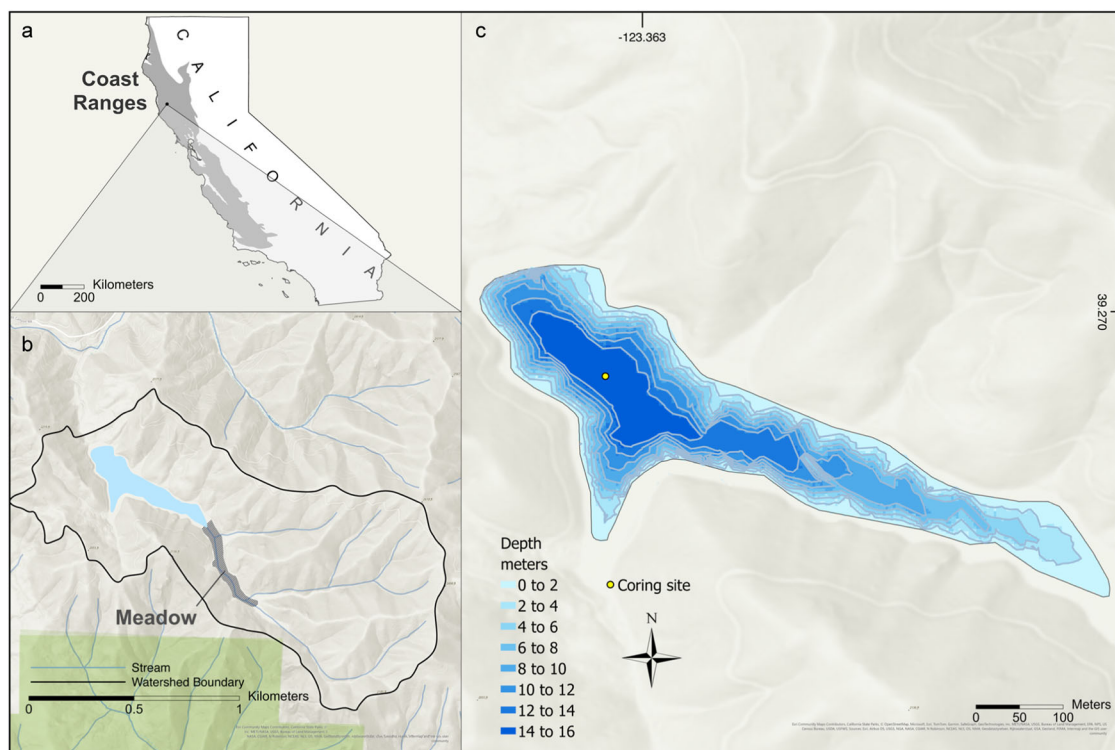


Fig. 1 | Location and geomorphic features around Leonard Lake. **a** Leonard Lake is situated in the northwestern Coast Ranges (dark gray shading)⁵⁷, California, USA⁵⁸. **b** Streams (blue lines)⁵⁹ and the watershed (black line) are depicted around Leonard Lake (light blue) and its meadow (dark gray), with the world hillshade map layer⁶⁰.

c Bathymetric map of Leonard Lake where increasing depth (m) is shown by increasingly dark blues, and the coring site is shown by a yellow circle in the lake's depocenter. Copyright © 2024 Esri and its licensors. All rights reserved.

sediments of Leonard Lake; the model was then applied downcore. Our approach also incorporates time-uncertainty analysis, which is critical for quantitative interpretation of records in the paleosciences²⁸.

Results and discussion

Extreme precipitation deposits

Prominent light greenish-gray clay layers (10GY 7/1)²⁹ occur throughout the core, within a varying matrix of fine laminations and homogeneous zones (Fig. 2a, b). Finely laminated horizontal stratigraphy indicates deposition unimpacted by bioturbation. Downcore changes in grain size correspond to visually distinct stratigraphy such as clay layers and fine laminations (Fig. 2b, c). Fine laminations positively correspond with Fe/Al, which negatively correlates with homogenous zones (Fig. S1). In addition, high Si/Al values align with clay layers (Fig. 2d). Clay values above ~9% tend to produce a clay layer detectable to the naked eye and the correlation between Si/Al and percent clay is positive and significant ($r = 0.30$, $p = 0.02$, where autocorrelation was accounted for with the isospectral approach). Clay percentage data from the section of the core corresponding to the instrumental period encompass most of the range of percentage values present in the record from -550 CE to present; however, between -1050 to -550 CE, percent clay values exceed the highest values from the instrumental period. Measurements of Si/Al from the instrumental period encompass almost the entire range of variability over the full record; outside of the calibration period, only 2% of the values are higher than the Si/Al value in 1950 CE and none are lower than 1990 CE (Fig. 3a). Principal component analysis verifies trends in correlations, that is, grouping of siliciclastic elements (Si, Ti, Al, K); it also shows grouping of organic matter with Br on PC1 and the primary control of PC2 by Fe (Fig. S2, and additional sensitivity analysis in Fig. S3).

Correlation and proxy calibration

Of the proxies, Si/Al is most strongly correlated with integrated vapor transport (IVT, $\text{kg m}^{-1} \text{s}^{-1}$) data ($r_{\text{median}} = 0.63$, $p_{\text{median}} = 0.02$), where all

ensemble-member correlations are significant, and p values were corrected to account for false discoveries³⁰ (Fig. 3a, b; Fig. 4a). Strong, significant associations were also found between Si/Al and integrated water vapor (IVW; $r_{\text{median}} = 0.48$, $p_{\text{median}} = 0.09$) with significant ensemble-member correlations 96% of the time (Fig. 4b). Correlations between clay, IVT, and IVW are presented in the Supplementary Note 2 (Fig. S4a, b). Correlations between Si/Al and clay with Russian River (USGS station no. 11461500, ~20 km from Leonard Lake) and Navarro River (USGS station no. 11468000, ~30 km from Leonard Lake) streamflow data³¹ were positive but not significant and are not considered further. Reconstructed IVT incorporates uncertainties in both the calibration regression statistics and the age model using an ensemble approach (Fig. 5a–e). The last occurrence of median IVT values as high as the modern period ($\sim 40,000 \text{ kg m}^{-1} \text{ s}^{-1}$) was before the onset of the Medieval warming in 950 CE, after which it appears to have declined for several centuries to the record's nadir of $\sim 27,500 \text{ kg m}^{-1} \text{ s}^{-1}$ in the 1500s (Fig. 5e). Median IVT rose with some fluctuation during the Little Ice Age (1300–1850 CE). The largest median peaks in IVT occur ca. -860 CE and -70 CE and were $\sim 44,000 \text{ kg m}^{-1} \text{ s}^{-1}$ (Fig. 5e).

Extreme precipitation over the late Holocene in California

Stratigraphic data from Leonard Lake show remarkable repeating patterns throughout the core that we interpret as hydrologically forced changes in the lake's depositional processes. Prominent clay layers are interspersed with fine laminations and/or homogenous packages and, in the lower part of the core, occasional sandy layers (Fig. 2a, b). These lithological data suggest a process whereby extreme precipitation related to ARs transports fine siliciclastic rich material to the depocenter. The largest area of the watershed drains into the southeastern corner of the lake via a creek that traverses ~300 meters of meadow prior to entering open water. This creek overtops its channel and floods the meadow during high precipitation events and the coring site/depocenter lies ~500 m from its mouth. As a result, coarser

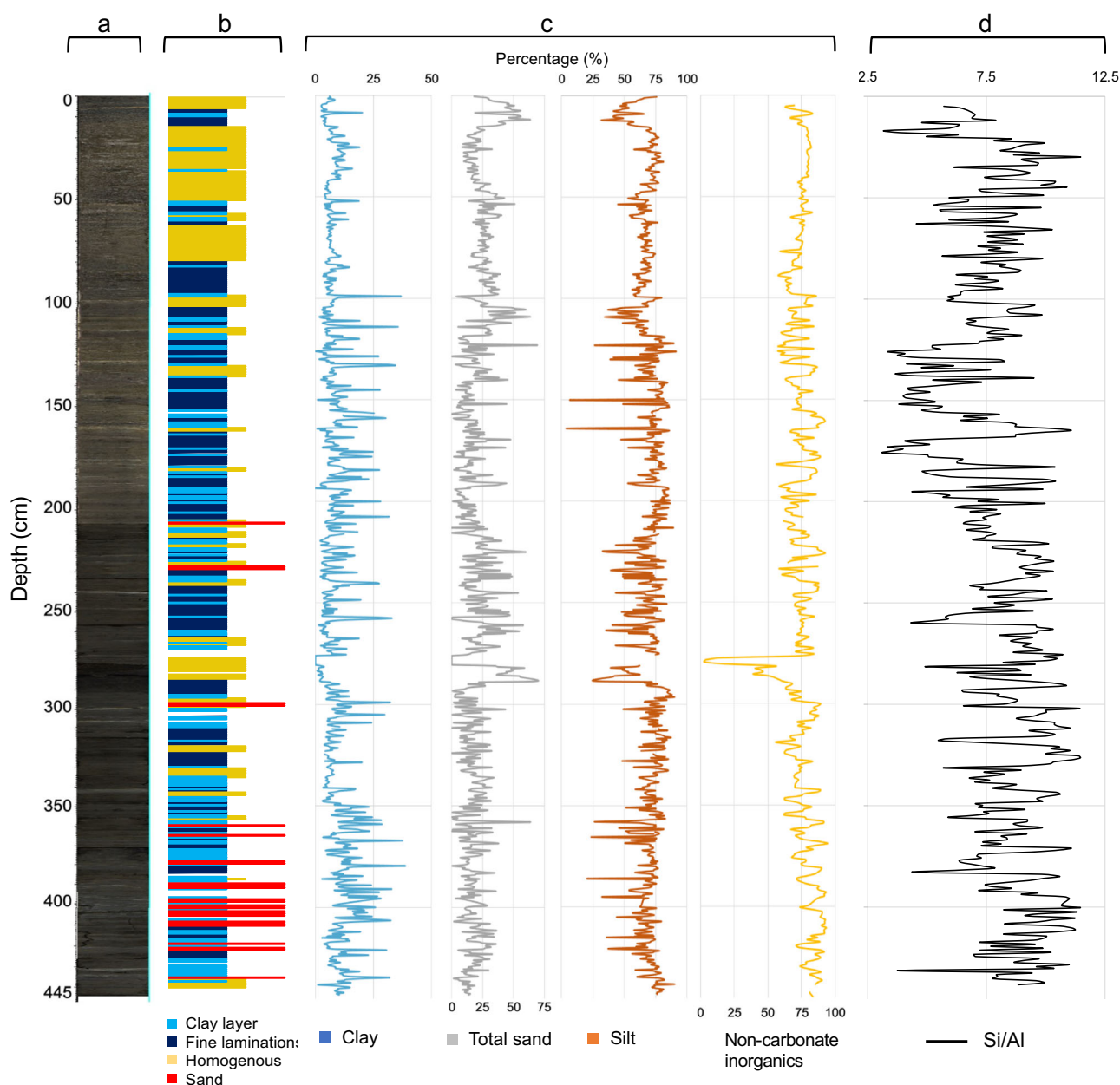


Fig. 2 | Lithological and geochemical results from Leonard Lake. Core analyses from Leonard Lake are plotted on the same depth scale (left): **a** Composite line scan imagery; **b** lithological descriptions based on visual analysis where clay layers are

blue, fine laminations are black, homogenous areas are yellow, and sand layers are red and; **c** percentage data for clay (blue), total sand (gray), silt (orange), and non-carbonate inorganics (yellow); and **(d)** Si/Al values (black).

material is not carried to the depocenter, but rather the clay fraction flushes into the lake and slowly settles out, with visible layers indicating periods of extreme precipitation. We note a dominant pattern of homogenous sediment followed by a clay layer, overlain by a section of fine laminations. Fine laminations (\leq mm scale) suggest suboxic to anoxic benthic conditions, allowing little degradation of organic matter and a lack of bioturbation. In addition, the correspondence between fine laminations and increased Fe/Al support the idea that sedimentary Fe was created in situ as a result of anaerobic decomposition (Fig. S1). This sequence suggests a process in which large storms raise lake levels, creating anoxic bottom water conditions that facilitate the preservation of fine laminations until (or unless) relatively dry conditions lowered lake levels. Dry conditions are likely recorded by homogenous packages that indicate oxygenated bottom waters and bioturbation. Modern lake level data from Leonard Lake support the underlying idea that large precipitation events appreciably raise lake levels while

dry conditions lower lake levels (Supplementary Note 3, Fig. S5). The presence of sandy layers in the lower portion of the core may have formed concurrent with lower lake levels during nascent formation. The shallow lake levels would likely result in discharge much closer to the coring site because the mouth of the creek extended further into the basin. Consequently, coarser material could be more readily carried to the depocenter during high energy events.

Our evidence supports the premise that Leonard Lake consistently registered extreme precipitation over a 3200-year period. Faithful recording of extreme precipitation as clay deposition has allowed a quantitative reconstruction of AR-related metrics in the late Holocene, the first of its kind for the western United States. The reconstructed median IVT suggests the most recent analogue to modern extreme precipitation occurred over a millennia ago and that since 1300 CE there has been an upward trend. As a key metric of ARs, the IVT reconstruction indicates California has been

subject to pluvial episodes that exceed any in the meteorological instrumental era, with the largest episodes occurring two and three millennia ago.

Based on inferences from proxy records, Northern Hemisphere mid-latitude net precipitation has increased since 8 ka³² and midlatitude Northern Hemisphere models show storm activity has increased since 10 ka³³. The early to middle Holocene was drier and a potential driver of these conditions was a weaker latitudinal temperature gradient. A weaker latitudinal gradient has again developed under anthropogenic warming; it has been argued that this could be consistent with future aridity and a

reduction in mid-latitude water resources³². Our reconstruction appears to show that AR activity may not be linked to the northern hemisphere temperature gradient. In contrast, we find a slight decreasing trend in IVT values between -1300 and 1500 CE (Fig. 5e) while the latitudinal temperature gradient was strong, and an increasing trend in IVT values between 1500 CE and the present day (Fig. 5e) as the latitudinal temperature gradient weakened. The difference between our record's trends and others³² may simply reflect the fact that ARs are distinct features of the hydroclimate that are not interchangeable with net precipitation. Differences could also be related to sub-regional variability detected by our site and/or changes in temperature and insolation gradients, such as the role of cooler tropical Pacific sea surface temperatures and North American aridity³⁴. Nevertheless, our work is consistent with recent model output comparing midlatitude landfalling ARs in western North America between the mid-Holocene and the preindustrial period³⁵. This research shows a drying trend in annual AR precipitation between the two periods, which is supported by the decreasing IVT trend in our record before the preindustrial era, and is attributed to decreased atmospheric vapor content related to decreasing summer insolation³⁵. Thermodynamic considerations, such as increased AR vapor content due to warmer air and sea surface temperature, are expected to predominantly drive increases in the number of ARs in the future³⁶. Mechanism(s) notwithstanding, these data provide a critical perspective to improve the precision and accuracy of risk assessments for precipitation related threats, such as enhanced flash flooding or debris flow¹³.

Leonard Lake data align with regional climate reconstructions and suggest the reliability of Si/Al to record both periods of increased precipitation as well as drought (Fig. S6a-c). For example, we find increasing IVT during the Little Ice Age consistent with cooler and wetter climatic expectations. Heavy precipitation, as reconstructed from blue oak tree rings in northern California, also suggest an increase in the frequency or intensity of ARs in northern California since the 1700s³⁷ (Fig. S6a). Our reconstruction also indicates decreasing IVT during the Medieval Climate Anomaly, a period characterized by centennial-scale aridity in the North American West³⁷. Our reconstruction shows several eras of low IVT occurring in 600-725 and 1250-1350 CE, as well as the 1500 s—the latter of which is concurrent with the widespread 16th century mega-drought^{38,39}. A reconstruction of Sacramento River flows found the driest 20-year period was in the early 1300s⁴⁰, aligning with the low IVT reconstructed in this study between 1250-1350 CE. The Sacramento River flow record⁴⁰ also shows some of the driest individual years occurred in the early 1500 s (Fig. S6b). The consensus across multiple records lends credence to our reconstruction. Although our record cannot reconstruct specific storm

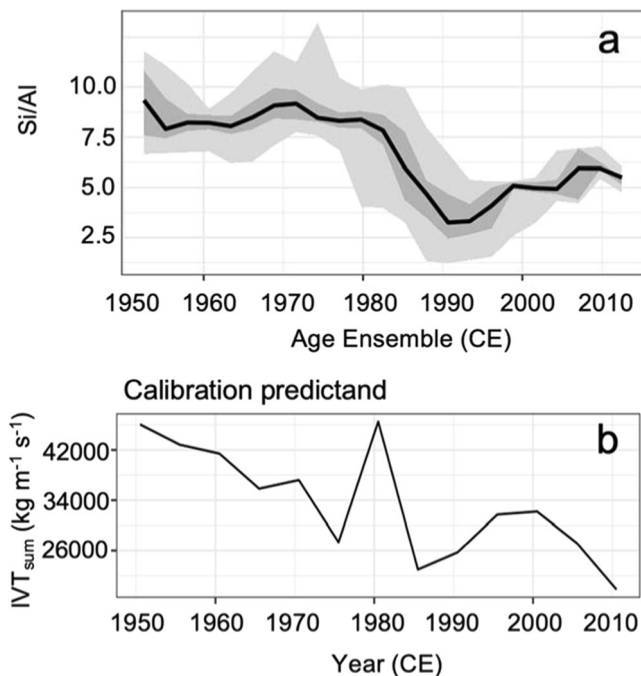


Fig. 3 | The proxy data (Si/Al) and instrumental data (IVT) during the calibration period. **a** The graph shows variation in Si/Al with age uncertainty bands; the median estimate is shown as a solid black line and the 50 and 95% highest probability density regions are shown in dark and light gray. **b** The graph shows the calibration-in-time predictand where the y-axis is annually summed IVT (kg m⁻¹ s⁻¹) and binned at a 5-year interval.

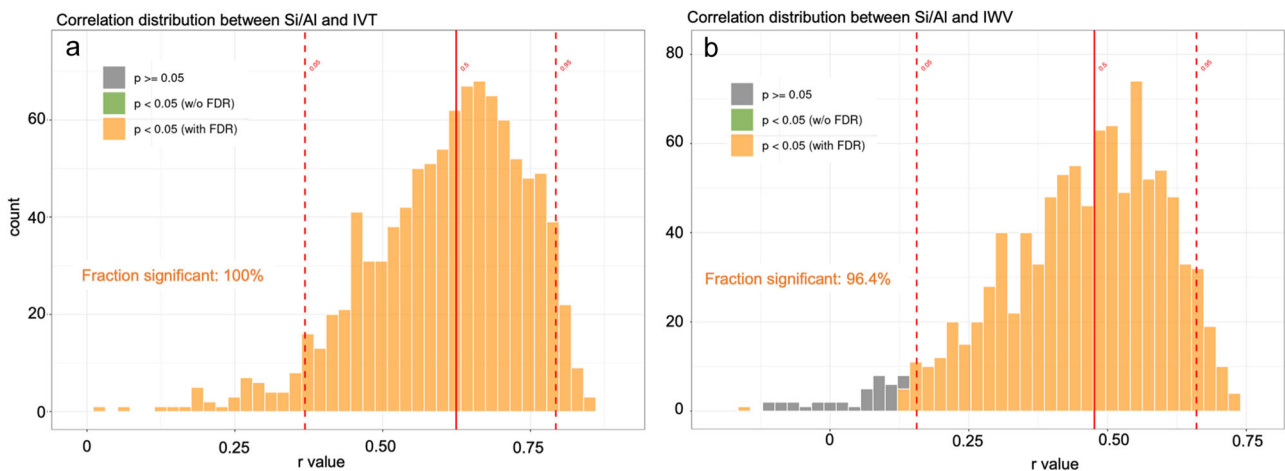


Fig. 4 | Correlation distributions of Si/Al and IVT and Si/Al and IWV and their significance. **a** The distribution of Si/Al and IVT and **(b)** the distribution of Si/Al and IWV using the “effective-n” approach^{38,53} with the false discovery rate (FDR) controlled. The ensemble count is on the y-axis and the r value is on the x-axis. In **(a)**,

the median r value (0.63) is shown by the vertical red line and the 0.05 and 0.95 percentile r values are shown by dashed red lines. In **(b)**, the median r value (0.48) is shown by the vertical red line and the 0.05 and 0.95 percentile r values are shown by dashed red lines.

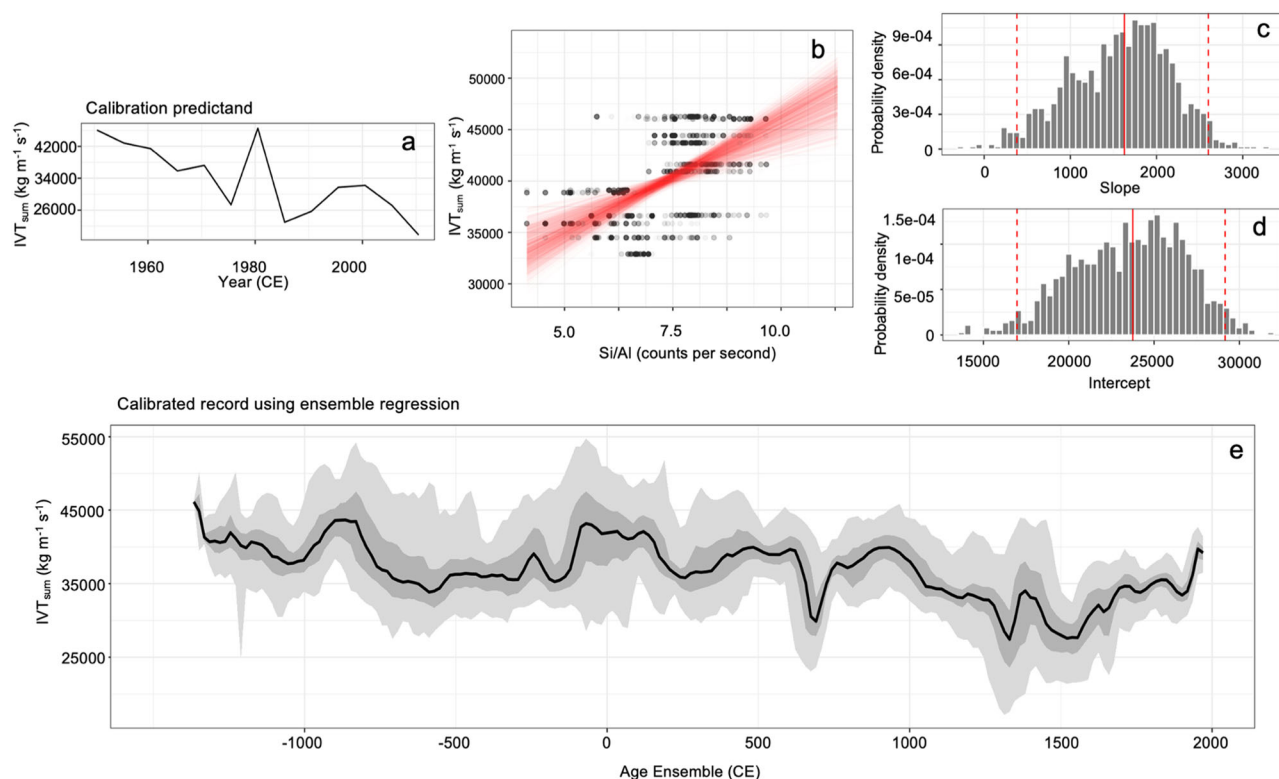


Fig. 5 | Calibrated reconstruction of paleo-IVT using ensemble regression. **a** The graph shows the calibration-in-time predictand. **b** The scatterplot shows the relation between Si/Al and IVT with points from 100 age ensemble members plotted with transparency and ensemble models plotted as partially transparent red lines. The right panel shows the distribution of the regression model (**c**) slope and (**d**) shows the

intercepts, where vertical red lines indicate the 50th (solid), 2.5th, and 97.5th (dashed) percentiles. **e** The graph shows reconstructed IVT using age ensembles and regression model ensembles. The median estimate is shown as a solid black line and the 50 and 95% highest probability density regions are shown in dark and light gray.

events, the alignment with these broader climate trends highlights the importance of extreme precipitation in driving pluvial/drought cycles in California going back millennia.

Although the uncertainty analysis in this work considered a range of Si/Al—AR linkages, we cannot account for the possibility that the relationship between Si/Al and extreme precipitation changed through time (non-stationarity), a problem besetting all paleo-reconstructions. Other variables that may affect siliclastic transport and preservation within the sedimentary archive include the changes in lake level mentioned above and vegetation changes that alter run-off to the site. However, we suggest that the processes influencing Si/Al and clay content at Leonard Lake have been sufficiently stable to support a consistent proxy signal for millennia. Leonard Lake is situated in the ancestral territory of the Pomo Tribe. Tribal members call this lake *Ka-su²-su*, meaning waters malevolent or waters bedeviled, likely due to the extremely steep shore and surprising depth; Indigenous people are thought to have avoided using the lake and surrounding area⁴¹. Hence, there is evidence the lake has long been deep and the area relatively undisturbed. In the recent past, the old-growth redwood forests in Leonard Lake's watershed have been protected by the landowners, unlike the surrounding area which experienced heavy logging⁴¹. The relatively constant sedimentation rate and lack of obvious major sedimentological changes also supports the idea of long-term stability.

The recognition that a paleo perspective is necessary to accurately understand the risks associated with extreme events¹³ continues to motivate research concerning the long-term hydrologic history of the western United States. Evidence from this study suggests that paleo records of AR activity are detectable given the right long-term depositional environment, such as is found at Leonard Lake. Our reconstruction corresponds with recognized paleoclimatic periods including the Medieval Climate Anomaly and Little Ice Age, corroborates regional tree ring reconstructions, and is consistent with a mega-drought event. Importantly, these findings show that extreme

precipitation events have been a mechanism driving both pluvial and drought conditions in California for at least 3200 years. This study contextualizes present day storms by demonstrating the range of AR-related extreme precipitation on millennial time scales in the hydrologically dynamic area of California.

Methods

In April 2014, two surface cores and three sets of overlapping long cores were recovered from the depocenter of Leonard Lake. Bolivia and Livingston corers were used to obtain overlapping cores with a total length of 446 cm. Core liners were used to preserve stratigraphic integrity and to aid core transport and sampling. All cores were split, described, imaged, and sub-sampled in the Quaternary Paleoenvironmental Research Laboratory at the U.S. Geological Survey in Menlo Park, California. Lake depth measurements were collected with a Norcross H22PX[®] and geolocated with a Trimble GeoXH[®] to create a bathymetric map (Fig. 1c).

Geochronology

A total of 17 samples of discrete organic materials were obtained for AMS ¹⁴C dating and were processed at the National Ocean Sciences Accelerator Mass Spectrometry center at Woods Hole Oceanographic Institution, the US Geological Survey Radiocarbon Laboratory, and Beta Analytic (Table S1). We note the date at 236 cm represents an age reversal and was treated as an outlier by the model. Given that the two proximal dates at 237.5 cm and 244.5 cm overlap at an uncertainty of two sigma, we deem the exclusion of the date at 236 cm as justifiable. Short-lived radionuclides (²¹⁰Pb, ¹³⁷Cs, and ²²⁶Ra) from the upper 60 cm were measured using gamma spectrometry⁴² (Table S2). Seventeen samples were measured until unsupported ²¹⁰Pb was no longer detected and a definitive peak ¹³⁷Cs was found. Counting times of 48 to 72 h were generally required to reach a statistical error of less than 10% for excess ²¹⁰Pb in the deepest samples.

Excess ^{210}Pb was calculated as the difference between total ^{210}Pb and ^{226}Ra activities. Downcore ^{137}Cs values show a peak at 28 cm (Table S2), indicating fallout from nuclear weapons testing in 1963 CE. Background ^{210}Pb was likely reached around 50 cm, given the low and static dpm/g of the deepest ^{210}Pb measurements (Table S2). These data were used to construct the age-depth model (Fig. S7a, b) using the Bayesian software *Plum* (version 0.3.0 using default priors)⁴³, in RStudio⁴⁴. In *Plum*, Monte Carlo age-depth fitting uses calibrated-age probability distributions, enabling uncertainty calculations at every level.

To understand the effect of age model uncertainty on our results, the *geoChronR* package in R was used to propagate error and visualize results³⁸. Radiometric data and proxy data were reformatted into a Linked PaleoData (LiPD) dataset. *GeoChronR* requires users to run one of four age-modeling techniques, of which the algorithm in *Bacon* most closely aligns with our approach^{45,46} (*Plum* is not available in *geoChronR*). The underlying process is as follows: within *geoChronR*, *Bacon* is run normally and returns a subset of the Markov Chain Monte Carlo accumulation rate ensemble members with high *a posteriori* probabilities; then, an age ensemble—a composite of 1000 highly probable age models—is extracted for analyses. To incorporate ^{210}Pb error in our analyses, we ran *Bacon* with seventeen modeled ^{210}Pb ages and their associated uncertainties from *Plum* (Fig. S8, Table S3) as well as ^{14}C data. Both the *Plum* and *Bacon* models produced highly similar age estimates (average of 3.3% difference; Fig. S9) for the full age models, justifying this approach. The mean deposition time over the entire core is 7.4 year cm^{-1} with a mean of 1.98 year cm^{-1} during the calibration period (1948–2015 CE). Average model uncertainty is ± 74.5 year over the 3200-year-long core, while average uncertainty through the calibration period is ± 3.5 year.

Stratigraphic, grain size, and geochemical analyses

The sediment was described, at 0.5-cm resolution, as one of four types: clay layers, fine laminations, homogenous deposition, and sand layers. Grain size measurements were carried out contiguously at 0.5-cm resolution. Samples were processed first with 50 mL of bleach (5.25% sodium hypochlorite) for 24 h to remove organic material, water washed, and then treated with 10% HCl to remove carbonates. Analysis was conducted on a Beckman Coulter LS13 320 Laser Diffraction Particle Size Analyzer in the Unsaturated Flow Processes laboratory at the U.S. Geological Survey. Water content at 50 °C, loss on ignition (LOI) at 550 °C (organic matter), and at 960 °C (carbonate) were determined at 1-cm contiguous intervals⁴⁷; the residual is quantified as the non-carbonate inorganic fraction. A Thermo Scientific Niton XL3t GOLDD portable XRF (p-XRF) was used to collect 1-cm resolution elemental data on split cores with standard reference materials: 165a⁴⁸, 2709a⁴⁹, and JMS-1 marine sediment⁵⁰.

Analyses and instrumental data

Principal component analysis (PCA) was undertaken on elemental and LOI datasets using compositional data analysis techniques^{51–53} (see Supplementary Methods and Supplementary Note 1). Pearson's correlation coefficients between proxy and instrumental data were calculated for each age ensemble^{28,54}. The false discovery rate was controlled³⁰. We calibrated the instrumental record of ARs with values of Si/Al and percent clay using age assignments derived from the age-depth model for each sample depth and regressing these against the dataset of AR metrics²⁵, following established protocol²⁶.

A key feature of ARs is that they move large amounts of water vapor. Hence, metrics that incorporate moisture and wind best reflect this water vapor flux²⁵. ARs have been defined by vertically integrated horizontal vapor transport (IVT, $\text{kg m}^{-1} \text{s}^{-1}$) and integrated water vapor (IWV, kg m^{-2}) exceeding defined thresholds⁵. As such, we calculated an annual sum for both IVT and IWV for ARs that were specified at 40°N in Gershunov's²⁵ database⁵⁵. We then calibrated our proxy data to these sums. For each iteration in the analysis, an age ensemble-member was selected and used to bin the Si/Al (or clay data) onto a 5-year interval where data were averaged. The instrumental AR data were also binned at the same timescale. Streamflow data ($\text{ft}^3 \text{sec}^{-1}$) from stream gages in two local rivers, the Russian

River (USGS station no. 11461500) and Navarro River (USGS station no. 11468000)³¹, were summed annually between 1950–2014 and considered along with the instrumental AR data. Within *geoChronR*, a linear regression model was derived, and then proxy data were scaled to guard against slope attenuation (“regression dilution”)⁵⁶. The model was used to reconstruct integrated vapor transport (IVT_{sum} , $\text{kg m}^{-1} \text{s}^{-1}$) from proxy data back in time, with age uncertainty propagated through the regression.

Data availability

Radiometric data (also provided in the supplementary information, see Tables S1 and S2), bathymetric data, and proxy data (elemental data, core physical property data, grain size data, and reconstructed IVT values) are available through the U.S. Geological Survey ScienceBase data release at <https://doi.org/10.5066/P1ECT7AM61>.

Received: 4 December 2023; Accepted: 29 March 2024;

Published online: 25 April 2024

References

- Zhu, Y. & Newell, R. E. A proposed algorithm for moisture fluxes from atmospheric rivers. *Mon. Weather Rev.* **126**, 725–735 (1998).
- Ma, W., Chen, G. & Guan, B. Poleward shift of atmospheric rivers in the southern hemisphere in recent decades. *Geophys. Res. Lett.* **47**, e2020GL089934. (2020).
- Ralph, F. M. et al. Flooding on California's Russian River: role of atmospheric rivers. *Geophys. Res. Lett.* **33**, L13801 (2006).
- National Oceanic and Atmospheric Administration (NOAA) Atmospheric Rivers: what are they and how does NOAA study them? Accessed April 2023; <https://www.climate.gov/news-features/feed/atmospheric-rivers-what-are-they-and-how-does-noaa-study-them#:~:text=NOAA%20studies%20atmospheric%20rivers%20to%20improve%20forecasting%20capabilities,moist%20air%20from%20the%20tropics%20to%20higher%20latitudes> (2023).
- Neiman, P. J., Ralph, F. M., Wick, G. A., Lundquist, J. D. & Dettinger, M. D. Meteorological characteristics and overlaid precipitation impacts of atmospheric rivers affecting the west coast of North America based on eight years of SSM/I satellite observations. *J. Hydrometeor.* **9**, 22e47 (2008).
- Dettinger, M. D. Historical and future relations between large storms and droughts in California. *San Fran. Est. Watershed Sci.* **14**, 1–22 (2016).
- Center for Western Weather and Water Extremes. Atmospheric River Scale Forecast Products. Accessed April 2023; <https://cw3e.ucsd.edu/arscale/> (2023).
- California Department of Water Resources. Harnessing Series of Winter Storms, California Increases State Water Project Allocation. Accessed June 2023; <https://water.ca.gov/News/News-Releases/2023/March-23/Harnessing-Series-of-Winter-Storms-California-Increases-State-Water-Project-Allocation> (2023).
- Tinker, R. U. S. Drought Monitor: California. Accessed April 2023; <https://droughtmonitor.unl.edu/CurrentMap/StateDroughtMonitor.aspx?CA> (2023).
- California Governor's Office of Emergency Services. 2023. 2023 Flood Recovery. Cal OES News. Accessed June 2023; <https://news.caloes.ca.gov/2023-spring-flood-recovery/>.
- Dettinger, M. D. Climate change, atmospheric rivers, and floods in California—a multimodel analysis of storm frequency and magnitude changes. *J. Am. Water Res. Assoc.* **47**, 514–523 (2011).
- Huang, X., Swain, D. L. & Hall, A. D. Future precipitation increase from very high resolution ensemble downscaling of extreme atmospheric river storms in California. *Sci. Adv.* **6**, eaba1323 (2020).
- Huang, X. & Swain, D. L. Climate change is increasing the risk of a California megaflood. *Sci. Adv.* **8**, eabq0995 (2022).
- Wilhelm, B. et al. Recent advances in paleoflood hydrology: from new archives to data compilation and analysis. *Water Secur.* **3**, 1–8 (2018).

15. Sabatier, P. et al. A review of event deposits in lake sediments. *Quaternary* **5**, <https://www.mdpi.com/2571-550X/5/3/34> (2022).
16. Kirby, M. E., Patterson, W. P., Ivanovici, L., Sandquist, D. & Glover, K. C. Evidence for a large middle Holocene flood event in the Pacific southwestern United States (Lake Elsinore, California), in *From Saline to Freshwater: The Diversity of Western Lakes in Space and Time* (eds Starratt, S. W. & Rosen, M. R.) Vol 536 (Geological Society of America Special Paper, 2018).
17. Street, J. H., Anderson, R. S. & Paytan, A. An organic geochemical record of Sierra Nevada climate since the LGM from Swamp Lake, Yosemite. *Quat. Sci. Rev.* **40**, 89–106 (2012).
18. Kirby, M. E., Zimmerman, S. R. H., Patterson, W. P. & Rivera, J. J. A 9170-year record of decadal-to-multi-centennial scale pluvial episodes from the coastal Southwest United States: a role for atmospheric rivers? *Quat. Sci. Rev.* **46**, 57–65 (2012).
19. Blunt, A. B. & Negrini, R. M. Lake levels for the past 19,000 years from the TL05-4 cores, Tulare Lake, California, USA: geophysical and geochemical proxies. *Quat. Int.* **387**, 122–130 (2015).
20. Metcalfe, S. E., Jones, M. D., Davies, S. J., Noren, A. & MacKenzie, A. Climate variability over the last two millennia in the North American Monsoon region, recorded in laminated lake sediments from Laguna de Juanacatlan, Mexico. *The Holocene* **20**, 1195–1206 (2010).
21. Van Daele, M. et al. The 600 yr eruptive history of Villarrica Volcano (Chile) revealed by annually laminated sediments. *Geol. Soc. Am. Bull.* **126**, 481–498 (2014).
22. Hendy, I. L., Napier, T. J. & Schimmelmann, A. From extreme rainfall to drought: 250 years of annually resolved sediment deposition in Santa Barbara Basin, California. *Quat. Int.* **387**, 3–12 (2015).
23. Du, X., Hendy, I. & Schimmelmann, A. A 9000-year flood history for Southern California: a revised stratigraphy of varved sediments in Santa Barbara Basin. *Marine Geology* **397**, 29–42 (2018).
24. Thompson, L. C., Dewees, C. M. & Dewees, C. M. *Limnology and fish of Leonard Lake, Mendocino County, California. Wildlife, Fish, and Conservation Biology Department*, p. 17 (UC Davis, 2009).
25. Gershunov, A., Shulgina, T., Ralph, F. M., Lavers, D. A. & Rutz, J. Assessing the climate-scale variability of atmospheric rivers affecting western North America. *Geophys. Res. Lett.* **44**, 7900–7908 (2017).
26. Grosjean, M., von Gunten, L., Trachsel, M. & Kamenik, C. Calibration-in-time: transforming biogeochemical lake sediment proxies into quantitative climate variables. *Pages News* **17**, 108–110 (2009).
27. von Gunten, L., Grosjean, M., Kamenik, C., Fujak, M. & Urrutia, R. Calibrating biogeochemical and physical climate proxies from non-varved lake sediments with meteorological data: Methods and case studies. *J. Paleolim.* **47**, 583–600 (2012).
28. McKay, N., Emile-Geay, J. & Khider, D. GeoChronR—an R package to model, analyze and visualize age-uncertain paleoscientific data. *Geochronology* **3**, 149–169 (2021).
29. Munsell Color. *Munsell Soil Color Charts: with Genuine Munsell Color Chips* (Munsell Color, Grand Rapids, MI, 2010).
30. Benjamini, Y. & Hochberg, Y. Controlling the false discovery rate: a practical and powerful approach to multiple testing. *J. Royal Stat. Soc. Ser. B* **57**, 289–300 (1995).
31. U.S. Geological Survey. USGS water data for the Nation: U.S. Geological Survey National Water Information System database, accessed September 2023 at; https://waterdata.usgs.gov/nwis/uv?site_no=11468000&legacy=1 (Navarro), https://waterdata.usgs.gov/nwis/uv?site_no=11461500&legacy=1 (Russian River). (2023).
32. Routson, C. C. et al. Mid-latitude net precipitation decreased with Arctic warming during the Holocene. *Nature* **568**, 83–87 (2019).
33. Jackson, C. S. & Broccoli, A. J. Orbital forcing of Arctic climate: mechanisms of climate response and implications for continental glaciation. *Clim. Dyn.* **21**, 539–557 (2003).
34. Shin, S.-I., Sardeshmukh, P. D., Webb, R. S., Oglesby, R. J. & Barsugli, J. J. Understanding the Mid-Holocene climate. *J. Clim.* **19**, 2801–2817 (2005).
35. Skinner, C. B., Lora, J. M., Payne, A. E. & Poulsen, C. J. Atmospheric river changes shaped mid-latitude hydroclimate since the mid-Holocene. *Earth Plan. Sci. Lett.* **541**, 116293 (2020).
36. Gao, Y. et al. Dynamical and thermodynamical modulations on future changes of landfalling atmospheric rivers over western North America. *Geophys. Res. Lett.* **42**, 7179–7186 (2015).
37. Howard, I. T. et al. A 440-year reconstruction of heavy precipitation in California from blue oak tree rings. *J. Hydrometeorol.* **24**, 463–477 (2023).
38. Trouet, V. et al. A 1500-year reconstruction of annual mean temperature for temperate North America on decadal-to-multidecadal time Scales. *Environ. Res. Lett.* **8**, 024008 (2013).
39. Woodhouse, C. A. & Overpeck, J. T. 2000 years of drought variability in the central United States. *Bull. Am. Meteorol. Soc.* **79**, 2693–2714 (1998).
40. Meko, D. M., Therrell, M. D., Baisan, C. H. & Hughes, M. K. Sacramento River flow reconstructed to AD 869 from tree rings. *J. Am. Wat. Res. Assoc.* **37**, 1029–1039 (2001).
41. Brovarney, D. *Mendocino Refuge: Lake Leonard and Reeves Canyon*, p. 177 (Landcestry, Ukiah, California, 2022).
42. Van Metre, P. C. & Fuller, C. C. Dual-core mass-balance approach for evaluating mercury and ²¹⁰Pb atmospheric fallout and focusing to lakes. *Environ. Sci. Technol.* **43**, 26–32 (2009).
43. Aquino-López, M. A., Blaauw, M., Christen, J. A. & Sanderson, N. K. Bayesian analysis of ²¹⁰Pb dating. *J. Agric. Biol. Environ. Stud.* **23**, 317–333 (2018).
44. R. Core Team, R: A Language and Environment for Statistical Computing (R Foundation for Statistical Computing, Vienna, Austria), <https://www.R-project.org/> (2020).
45. Blaauw, M. & Christen, J. A. Flexible paleoclimate age-depth models using an autoregressive gamma process. *Bayesian Anal.* **6**, 457–474 (2011).
46. Reimer, P. et al. The IntCal20 northern hemisphere radiocarbon age calibration curve (0–55 cal kBP). *Radiocarbon* **62**, 725–757 (2020).
47. Dean, W. E. Determination of carbon and organic matter in calcareous sediments and sedimentary rocks by loss on ignition; comparison with other methods. *J. Sed. Res.* **44**, 242–248 (1974).
48. Standard Reference Material 165a, *Glass Sand*, National Institute of Standards and Technology, US Department of Commerce: Gaithersburg, MD (9 November 1992).
49. Standard Reference Material 2709a, *San Joaquin Soil*, National Institute of Standards and Technology, US Department of Commerce: Gaithersburg, MD (7 April 2009).
50. Terashima, S., Imai, N., Taniguchi, M., Okai, T. & Nishimura, A. The preparation and preliminary characterisation of four new Geological Survey of Japan geochemical reference materials: Soils, JSO-1 and JSO-2; and marine sediments, JMS-1 and JMS-1. *Geostand. Newsl.* **26**, 85–94 (2002).
51. Aitchison, J., Barceló-Vidal, C., Martín-Fernández, J. A. & Pawlowsky-Glahn, V. Logratio analysis and compositional distance. *Math. Geol.* **32**, 271–275 (2000).
52. Egozcue, J. J., Pawlowsky-Glahn, V., Mateu-Figueraz, G. & Barceló-Vidal, C. Isometric logratio transformations for compositional data analysis. *Math. Geol.* **35**, 279–300 (2003).
53. Filzmoser, P., Hron, K. & Reimann, C. Principal component analysis for compositional data with outliers. *Environmetrics* **20**, 621–632 (2009a).
54. Dawdy, D. R. & Matalas, N. C. Analysis of variance, covariance, and time series, in *Handbook of Applied Hydrology*, (ed Chow, V. T.) 8–68 (McGraw-Hill Book Co., New York, 1964).

55. SIO R1 Catalog. Catalog of landfalling atmospheric rivers along the western coast of North America. <https://weclima.ucsd.edu/data-products/> (2017).
56. Esper, J., Frank, D. C., Wilson, R. J. S. & Briffa, K. R. Effect of scaling and regression on reconstructed temperature amplitude for the past millennium. *Geophys. Res. Lett.* **32**, L07711 (2005).
57. Knight, C. A. Geochemical, grain size, lithological, bathymetric, reconstructed integrated vapor transport, and age model data for Leonard Lake, Mendocino County. ScienceBase. <https://doi.org/10.5066/P1ECT7AM> (2024).
58. Esri. California's physiographic regions. Accessed September 2023; <https://www.arcgis.com/home/item.html?id=f75eae4d5d6046b8b24f1d99415e44bd> (2021).
59. Esri. California Boundary TIGERLINE. Accessed September 2023; <https://www.arcgis.com/home/item.html?id=0f653a1cc53f4660b5cb407cb4d53337> (2019).
60. Esri. California Streams. Accessed September 2023; <https://www.arcgis.com/home/item.html?id=92b18d9e091d469fa69d256fb395b946> (2023).
61. Esri. World Hillshade tile layer. Accessed September 2023; <https://www.arcgis.com/home/item.html?id=1b243539f4514b6ba35e7d995890db1d> (2015).

Acknowledgements

This research project was supported by the U.S. Geological Survey Climate and Land Use Change Research and Development Program. We thank Shannon Jacobs, Jared Jacobs, and Sandra Marshall for supporting field work at Leonard Lake Reserve. We thank Scott Mensing, Nicholas McKay, and both anonymous reviewers. Lastly, we thank Jason Addison, Tripti Bhattacharya, Ellie Broadman, Roger Byrne, Alicia Cowart, Andrea Foster, Christopher Fuller, Jason Jiang, Kim Perkins, and Francis Smith for laboratory, instrument, and field assistance.

Author contributions

C.A.K.: Data acquisition, Formal analysis, Writing—Original draft & editing, Visualizations. L.A.: Conceptualization, Data acquisition, Supervision, Funding acquisition, Writing—Review & Editing. L.P.: Data acquisition, Visualization, Writing—Review & Editing. M.C.: Data acquisition, Writing—Review & Editing. D.W.: Conceptualization, Data acquisition, Supervision, Funding acquisition, Writing—Review & Editing.

Competing interests

The authors declare no competing interests.

Additional information

Supplementary information The online version contains supplementary material available at <https://doi.org/10.1038/s43247-024-01357-z>.

Correspondence and requests for materials should be addressed to Clarke A. Knight.

Peer review information *Communications Earth & Environment* thanks Paul Zander and Daniel Ibarra for their contribution to the peer review of this work. Primary Handling Editors: Ola Kwiecien and Aliénor Lavergne. A peer review file is available.

Reprints and permissions information is available at <http://www.nature.com/reprints>

Publisher's note Springer Nature remains neutral with regard to jurisdictional claims in published maps and institutional affiliations.

Open Access This article is licensed under a Creative Commons Attribution 4.0 International License, which permits use, sharing, adaptation, distribution and reproduction in any medium or format, as long as you give appropriate credit to the original author(s) and the source, provide a link to the Creative Commons licence, and indicate if changes were made. The images or other third party material in this article are included in the article's Creative Commons licence, unless indicated otherwise in a credit line to the material. If material is not included in the article's Creative Commons licence and your intended use is not permitted by statutory regulation or exceeds the permitted use, you will need to obtain permission directly from the copyright holder. To view a copy of this licence, visit <http://creativecommons.org/licenses/by/4.0/>.

This is a U.S. Government work and not under copyright protection in the US; foreign copyright protection may apply 2024